Thermomechanical Fatigue, Oxidation, and Creep: Part I. Damage Mechanisms

R.W. NEU and HUSEYIN SEHITOGLU

Isothermal fatigue tests and both out-of-phase and in-phase thermomechanical fatigue tests were performed in air and in helium atmospheres. A wide range of temperatures from 20 °C to 700 °C was considered in these tests on 1070 steel specimens. A procedure for inert atmosphere testing using encapsulated specimens is described. Results indicate that the fatigue lives are 2 to 12 times greater in helium than in air. Interrupted tests were performed to characterize the progression of damage in the material. Results indicate that oxidation-induced crack nucleation and crack growth are detrimental at high temperatures for isothermal and out-of-phase thermomechanical fatigue tests. In these tests, transgranular cracking is observed. However, creep-induced intergranular cracking is the dominant damage mechanism during in-phase thermomechanical fatigue tests.

I. INTRODUCTION

A. *Background*

AN understanding of the different micromechanisms which affect the behavior of materials under isothermal and thermomechanical loading conditions is needed. In early work, isothermal tests performed at various temperatures, mechanical strain ranges, and strain rates were used to estimate the life of members undergoing thermomechanical fatigue. However, isothermal tests may not capture many of the important damage micromechanisms which operate under strain-temperature conditions. Depending on the strain-temperature variation, extensive oxide rupturing, both at the surface and crack tips, and intergranular cracking have been observed. Life prediction equations should reflect these dominant damage mechanisms.

A test devised to study material damage under varying strain-temperature histories is called the thermomechanical fatigue (TMF) test. In this type of test, both the temperature and mechanical strain imposed on the specimen are controlled. In TMF testing, the phasing of the strain and the temperature can arbitrarily be varied; moreover, these tests may more closely simulate the strain-temperature history of an actual component. Researchers primarily have considered two baseline TMF tests with proportional phasings in the laboratory: out-of-phase (maximum strain at minimum temperature) and in-phase (maximum strain at maximum temperature).

Even though conventional isothermal fatigue life data at the maximum temperature of a TMF cycle have been used to predict TMF lives, many researchers have shown that nonconservative predictions can still result[1-6] with this approach. Moreover, isothermal fatigue life at the minimum temperature could be less than at the maximum temperature in certain nickel-based superalloys.[7] It is essential to compare TMF and isothermal fatigue data at similar strain rates so that time-dependent damage mechanisms in both cases correspond. In Part I of this paper, observations of damage will be described as well as the conditions which activate them. In Part II of this paper, a life prediction damage model will be developed that predicts isothermal and TMF cases in air and in helium.

Environmental damage and creep damage on the material contribute to fatigue damage at elevated temperatures. A number of oxidation damage mechanisms have been proposed. These include (1) enhanced crack nucleation and crack growth by brittle surface oxide scale cracking;[8,9,10] (2) grain boundary oxidation which results in intergranular cracking;[8,11,12] and (3) preferential oxidation of second-phase particles.[13] Oxidation and fatigue can interact, resulting in a life much less than either of them acting alone.

Many mechanisms have been proposed that explain creep-induced damage and creep-fatigue interactions. These include (1) coalescence of intergranular voids ahead of an advancing crack;[14,15] (2) a greater crack tip plastic zone, resulting from the summation of the plastic zones of voids ahead of a crack;[16] (3) grain boundary sliding initiating wedge-type cracks at grain boundaries[17] and at hard second-phase particles on the grain boundaries;[18] (4) grain boundaries acting as weak paths for flow localization and crack growth;[19] and (5) the modification of the crack tip strain fields in the absence of cavities.[20] It would be expected that a number of these creep mechanisms would operate under both isothermal and TMF conditions depending on the alloy.

At elevated temperatures, an oxide layer forms on the surface of the specimen. This layer experiences a mechanical strain which can result from one or a combination of the following: (1) strain from the applied mechanical loading in the material; (2) the mismatch in the thermal expansion coefficients among the different stoichiometries of the oxides and substrate;[21-24] (3) the load due to the volume difference between the substrate and the various oxides (*e.g.*, Fe_2O_3, Fe_3O_4, and FeO);[25-28] (4) geometry effects (convexity of surface, *etc.*);[29,30] (5) relative creep behavior between the oxide and substrate;[23] and (6) viscous sliding of the oxide segments on the metal substrate.[23,28] These mechanisms

R.W. NEU, Research Assistant, and HUSEYIN SEHITOGLU, Associate Professor, are with the Department of Mechanical and Industrial Engineering, University of Illinois, Urbana, IL 61801.

Manuscript submitted May 16, 1988.

could affect the morphology of the surface oxide as well as the growing oxide-induced crack. A tensile mechanical loading in the oxide above some critical fracture strain will cause the brittle oxide to fracture,[9,21,31,32] and a large compressive loading can cause buckling of the oxide[22] or complete spallation.[9,22,30,33,34] These fracture strains are on the order of 0.0004[35] and as low as 0.0002 for oxide failure under thermal shock conditions.[21] It has been found that tensile oxide fracture is especially detrimental for crack initiation and crack growth, because the repeated oxide fracture can channel crack growth into the substrate.[9,31] Consequently, out-of-phase TMF is especially detrimental, because the oxide is in tension at low temperatures when the oxide has insufficient ductility to prevent cracking.

One way to separate environmental damage from fatigue and creep damage is by performing tests in an inert or nonoxidizing atmosphere. A number of researchers[2,10,11,31,32,36–41] have performed tests on different materials under these conditions. Under conditions in which creep mechanisms are dominant compared to environmental interaction effects, the fatigue life in air is about the same as in an inert atmosphere.[31,36–38] However, when an environmental contribution exists, an increase in life of a factor of 2 to 20 is observed in a nonoxidizing atmosphere for smooth specimens compared to tests performed in air,[10,31,32,39–41] and, similarly, the crack growth rate may differ by 20 times.[11] Very few tests in inert atmospheres have been conducted under TMF conditions,[2] and no comparisons of air and nonoxidizing atmosphere results have been reported.

B. *Current Work*

In Part I of this paper, lives under isothermal fatigue, out-of-phase, and in-phase TMF in both air and helium environments are reported for 1070 steel. A procedure for performing both isothermal and thermomechanical fatigue tests in a helium atmosphere is described. The lives from helium tests are compared to their air counterparts under both isothermal and thermomechanical fatigue conditions. The two-bar structure was utilized to obtain variations of out-of-phase and in-phase strain-temperature histories. Several temperature ranges have been considered with the TMF testing. From an extensive study of the oxides using the scanning electron microscope (SEM), the various oxidation-induced crack growth characteristics are shown, and a distinction between two major types of oxide growth is given.

In Part II, a life prediction methodology is formulated and directly checked against experiments. This methodology has the capability of handling a variety of strain-temperature histories and is described as the summation of the fatigue, environmental, and creep damage components.

II. EXPERIMENTAL PROCEDURE

A. *Material and General Test Procedure*

The material investigated was 1070 steel with the chemical composition given in Table I. This steel is typically used in railroad wheels. Class U (unheat-treated) railroad wheel steel was used in this study. The microstructure consists of pearlite colonies about 40 μm in diameter and an average pearlite interlamellar spacing of 0.5 μm. Specimens were cut from the rim of a railroad wheel with the axis of the specimen parallel to the circumferential direction of the wheel. The machined specimens had a circular cross-section with a diameter of 7.62 mm (0.3 in.) and a gage length of 25.4 mm (1 in.).

All testing was performed using a 20 kip servo-hydraulic MTS fatigue machine. Specimens were heated by a 2.5 kW Lepel induction heater. The induction coil configuration was designed to minimize the temperature gradients in the gage section. The specimen was cooled by convection into ambient air; therefore, thermal gradients which could occur by forced coolings were not a factor. Type K thermocouples were spot welded to the specimen's gage section to provide a reading for temperature. The strain was measured with a (25.4 mm (1 in.)) MTS high-temperature extensometer utilizing quartz rods. Both the fatigue machine and the induction heater were controlled by a closed-loop computer system.

B. *Isothermal Tests*

Strain-controlled isothermal fatigue tests were performed at temperatures ranging from 20 °C to 700 °C, which is near the austenite transformation temperature. Three strain rates were investigated: 0.02, 0.002, and 0.0002 s^{-1}, and a wide range of mechanical strain ranges were considered (0.003 to 0.020). Most isothermal test specimens were heated using induction. In a few tests, specimens were heated using a resistance furnace (tubular split-type). Specimens used for comparing oxides were all tested using induction heating. All tests were run to failure, which was defined as a 50 pct load drop from the maximum load of the stable cycle.

C. *Thermomechanical Tests*

Both out-of-phase and in-phase TMF tests were performed using the two-bar structure.[42,43,44] Based on this model, strain-temperature histories may be simulated[44] on laboratory samples. For out-of-phase TMF (Figure 1(a)), bar 1 with area A_1, length l_1, and temperature T_1 is undergoing the strain-temperature cycling ($T_1 = T$, where T is shown as a function of time in Figure 1(b)), while bar 2 with area A_2, length l_2, and temperature T_2 remains elastic and isothermal at the minimum (constant) temperature. Applying equilibrium and compatibility conditions to this structure gives

$$\varepsilon_{mech} + \varepsilon_{th} = \varepsilon_{net} = -\frac{S}{(E_2 C)}$$

where S represents the stress on bar 1, E_2 is the elastic modulus of bar 2, and $C = (A_2 l_1)/(A_1 l_2)$ is a geometry factor that determines the level of constraint. In most of the out-of-phase TMF tests performed in this study, the stiffness of bar 2 is taken to be much greater than bar 1 (A_2/A_1 is very large), so that the net strain remains zero. Consequently, bar 1 simulates a strain-temperature history such that the mechanical strain is equivalent to the negative of the thermal strain. This is often referred to as "total constraint." In the experimental program,

Table I. Chemical Composition of 1070 Steel Given as Weight Percent

C	Mn	Si	Cu	Cr	P	S	Ni	Mo	Fe
0.70	0.72	0.29	0.09	0.07	<0.05	0.041	0.04	<0.02	balance

bar 1 represents the specimen in the fatigue machine, and the effects of bar 2 on bar 1 are determined by the controlling software.

For in-phase TMF, both bars undergo temperature cycling ($T_1 = T_2 = T$ as shown in Figure 1). From equilibrium and compatibility, the following are obtained:

$$\varepsilon_{mech} + \varepsilon_{th} = \varepsilon_{net} = -\frac{S}{(E_2 C)} + \varepsilon_{th}(l_2/l_1)$$

The in-phase TMF case considered in this testing program was $C \rightarrow \infty$ (A_2/A_1 is very large) and $l_1/l_2 = 1/2$. This particular in-phase history was chosen, since mechanical strain range is identical to that for the out-of-phase TMF case described above. The material response under out-of-phase and in-phase TMF cycles is shown in Figure 2. In these plots, the net strain, which is experimentally controlled, is separated into the mechanical strain and thermal strain components. In the out-of-phase TMF case, the maximum tensile stresses occur at the minimum temperature end, while in the in-phase TMF case, the material undergoes tensile stresses at the maximum temperature end. A discussion for using the two-bar structure for other loading conditions can be found in References 43 and 44.

Many temperature ranges were considered for the TMF laboratory tests so that temperature effects on damage mechanisms in TMF could be investigated. These include minimum temperatures of 150 °C, 400 °C, or 500 °C with maximum temperatures ranging from 400 °C to 700 °C. Strain rates for heating were approximately $1.6 \times 10^{-4}\ s^{-1}$ and for cooling were $5.0 \times 10^{-5}\ s^{-1}$, for an average strain rate of $1.0 \times 10^{-4}\ s^{-1}$.

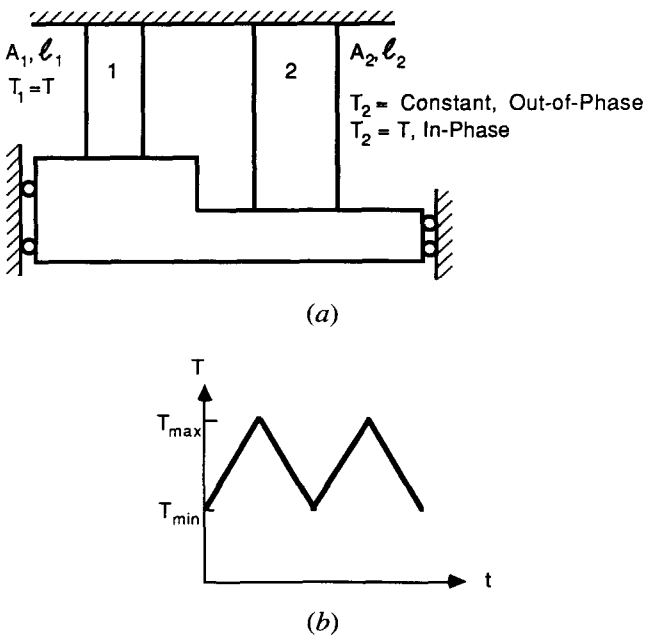

Fig. 1—(*a*) Schematic of the two-bar structure. (*b*) Temperature cycling imposed on bar 1 for both out-of-phase and in-phase TMF conditions and bar 2 for in-phase TMF conditions.

D. *Experiments in Helium Atmosphere*

Helium atmosphere tests were performed under both isothermal (two strain rates examined) and TMF conditions (both out-of-phase and in-phase examined). These test results are used to distinguish the creep damage from the oxidation damage. The method described below was developed to perform these inert atmosphere tests.

The reduced section of the specimen is sealed from the outside atmosphere with bellows, as shown in Figure 3. The center convolutions of the bellows are made of stainless steel and were included to provide flexibility. The remainder of the bellows is composed of INCONEL* tubes. Induction inherently heats the bellows to a greater extent than the specimen gage section; consequently, the bellows must be able to endure temperatures much higher than the testing temperature of the

*INCONEL is a trademark of the INCO family of companies.

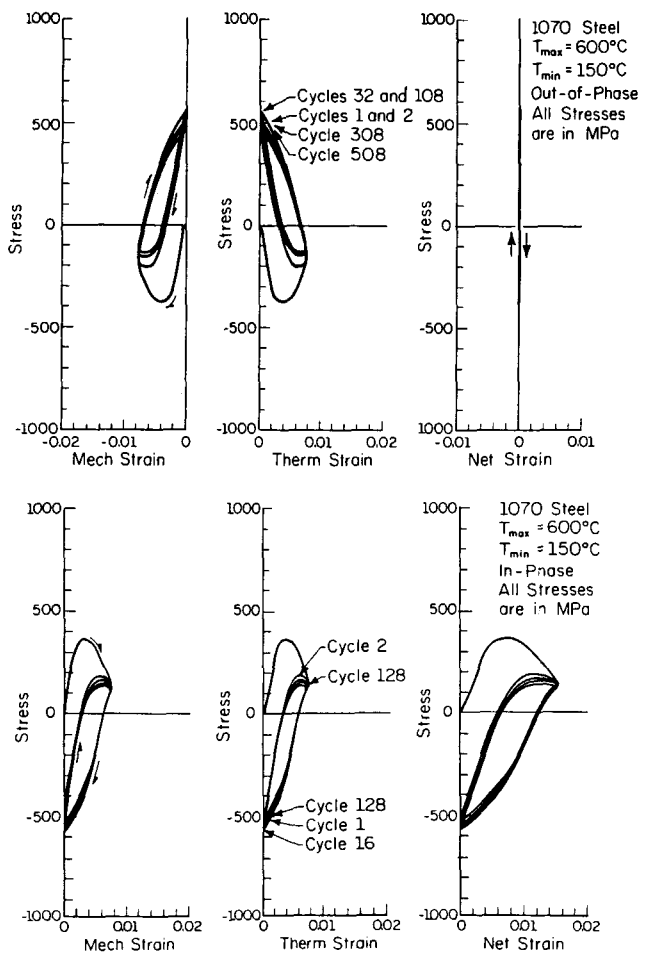

Fig. 2—Material response for two TMF conditions.

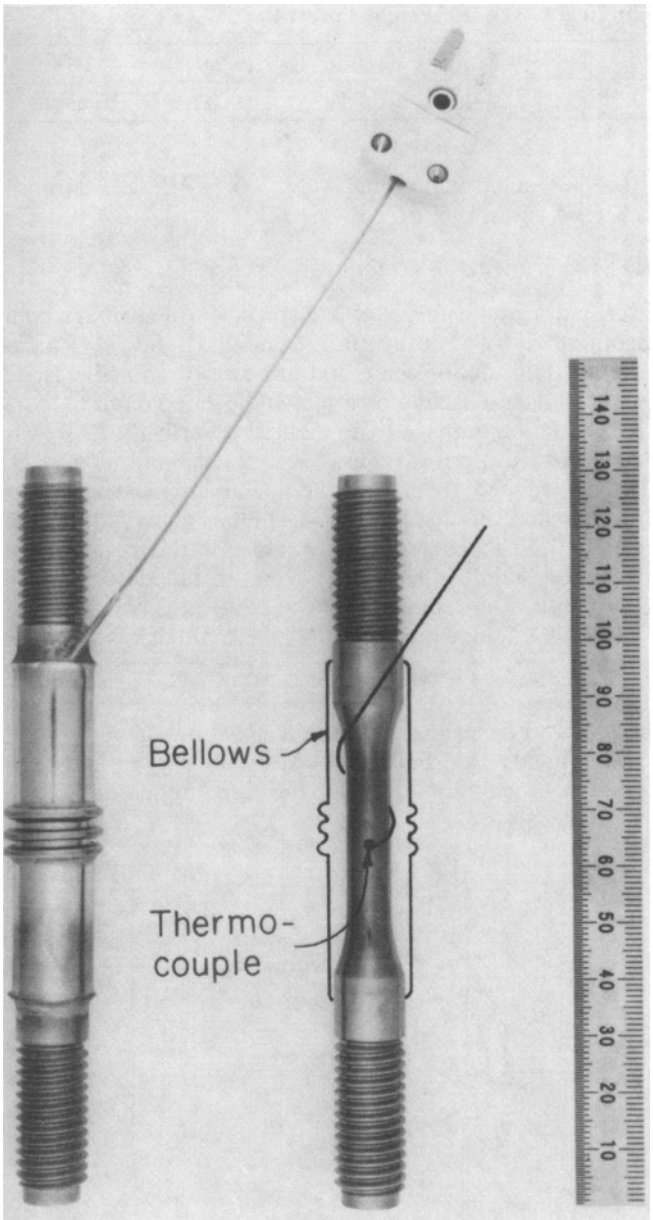

(*a*) (*b*)

Fig. 3—Specimen (*a*) with bellows and (*b*) schematic.

specimen. The heating in the gage section of the specimen is supplemented by the heat from the bellows.

Except for the last brazing operation, all of the brazing of the bellows to the specimen was done in a vacuum using either electron beam welding or induction heating. The final brazing operation was executed in a helium atmosphere at atmospheric pressure (approximately 1 atm). By this technique, the helium was sealed inside the bellows. A vacuum may instead be sealed inside the bellows in the same manner if desired; however, a vacuum did not transfer the heat produced in the bellows to the specimen and resulted in slower heating times (by a factor of 3). To determine the temperature of the specimen's gage length, the tip of a type K thermocouple with an INCONEL sheath was secured to the middle of the gage section with a thin metal strip. The thermocouple sheath can be seen coming out of the end of the bellows in Figure 3(a), and a schematic of its internal configuration is shown in Figure 3(b).

The induction coil used in the testing consisted of two symmetric coils with inner and outer wraps. Since most of the heat could only dissipate at the ends of the specimen, which was screwed into water-cooled grips, it was necessary to heat the ends of the gage section to a greater extent to maintain a uniform temperature within the gage section. Consequently, the coils were concentrated over the center of the INCONEL tubes of the bellows (Figure 3). They were adjusted on a specimen without bellows to minimize the temperature gradients in the 1 in. gage section of the specimen.

The strain was measured using a 2.5 in. extensometer utilizing quartz rods positioned on the specimen outside the bellows. A specimen without bellows was placed in the fatigue machine, and two high-temperature extensometers (1 in. and 2.5 in., in this case) were attached to either side of the specimen (Figure 4). Then the calibration was obtained by recording the strain in the 2.5 in. section ($\varepsilon_{2.5}$), while the strain in the 1 in. section ($\varepsilon_{1.0}$) was controlled.

The $\varepsilon_{2.5}$ and $\varepsilon_{1.0}$ levels are plotted against time, as shown for one of the calibrations in Figure 5. Note in Figure 5 that $\Delta\varepsilon_{2.5}$ was less than $\Delta\varepsilon_{1.0}$, because the $\Delta\varepsilon_{2.5}$ reading reflects the deflection at the shoulder of the specimen, where the strain is small and temperature is lower compared to the strain and uniform temperature in the gage section. The ramps produced by the 2.5 in. extensometer calibration were triangular with slight nonlinearity. Since the temperature gradient in the shoulder of the specimen was different at each testing temperature, it was necessary to repeat this calibration for each different temperature and strain range.

For TMF tests, temperature was cycled to obtain the desired calibration. For example, for a total constraint out-of-phase TMF test and an in-phase TMF test, the calibration for $\varepsilon_{2.5}$ is shown, along with the $\varepsilon_{1.0}$ strain, in Figure 6. The difference between $\varepsilon_{2.5}$ and $\varepsilon_{1.0}$ is due to the thermal strain outside the 1 in. gage section.

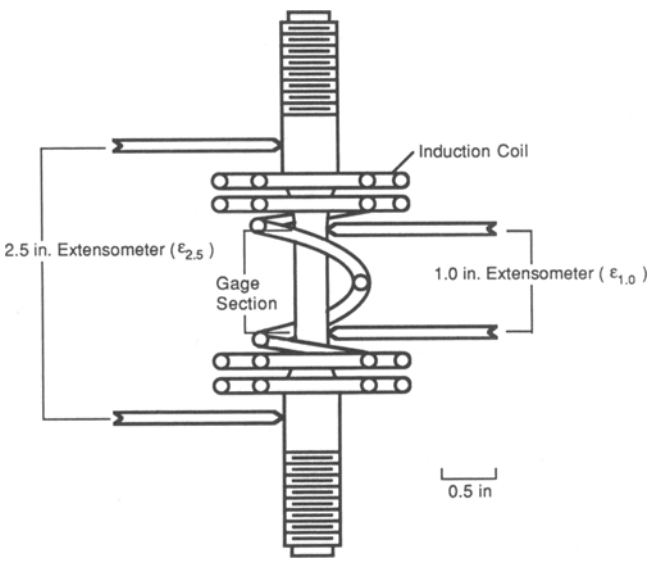

Fig. 4—Test configuration for helium calibration.

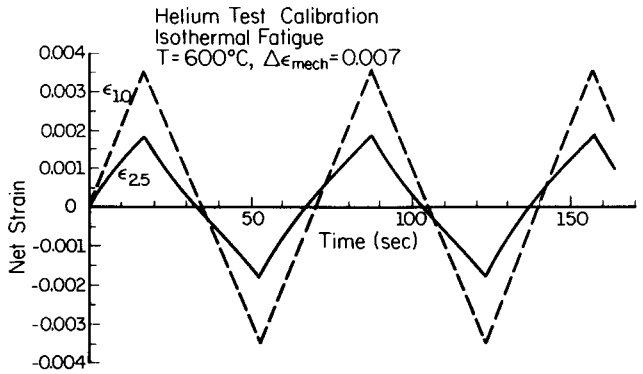

Fig. 5—Helium test calibration for isothermal fatigue.

Air tests (without bellows) were performed using the 2.5 in. extensometer and compared to air tests that had been performed using the 1 in. extensometer to determine the accuracy of this calibration. A comparison of these tests along with the results in helium is given in Table II. The fatigue lives in air obtained using the 1 in. and 2.5 in. extensometers are within acceptable scatter, especially when comparing the air results to the helium results, which showed a marked increase in life.

In addition, the isothermal fatigue calibrations were performed at $\dot{\varepsilon} = 0.0002\ s^{-1}$. These same calibrations were used for the high strain rate test ($\dot{\varepsilon} = 0.02\ s^{-1}$) shown in Table II. The calibrations were found not to be significantly affected by the strain rate, even at 600 °C, where 1070 steel response is strain rate sensitive. Therefore, it was not necessary to repeat this calibration for different strain rates at the same temperature.

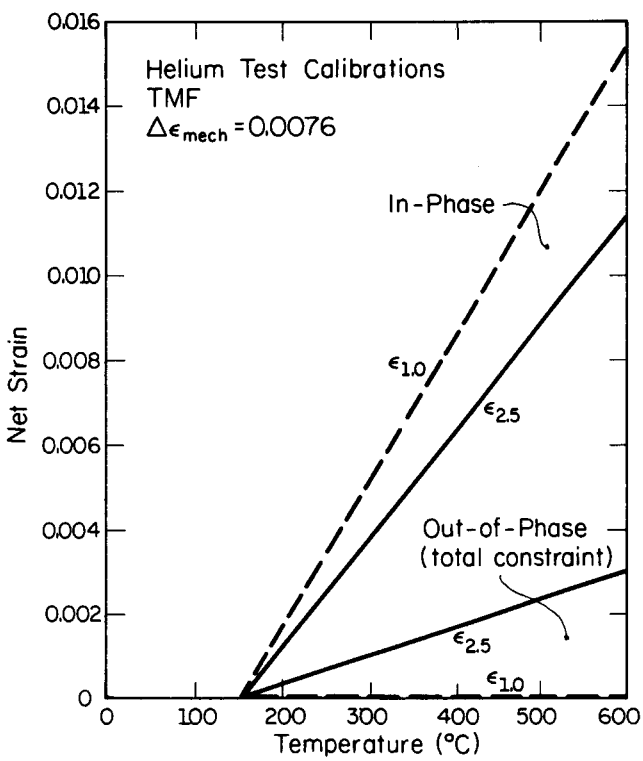

Fig. 6—Helium test calibration for TMF.

E. *Interrupted Tests*

To gain insight into the progression of damage during different phasing conditions, interrupted tests in air were performed. These tests involved using a number of specimens for each test condition and stopping each one at some percentage of failure life (*e.g.*, 10 pct N_f, 20 pct N_f, 40 pct N_f, 60 pct N_f, 80 pct N_f, and 100 pct N_f were used). Each specimen in these tests was sectioned and examined to measure the primary crack length and to detect microscopic damage. In particular, the oxide characteristics and oxide intrusion growth were examined, and the progress of internal creep damage along grain boundaries was also revealed. The specific tests used in this study were

(1) Isothermal fatigue, air, $T = 600$ °C, $\Delta\varepsilon_{mech} = 0.0070$, $\dot{\varepsilon} = 0.0002\ s^{-1}$, $N_f = 700$;
(2) Out-of-phase, total constraint TMF, air, $T = 150$ °C to 600 °C, $\Delta\varepsilon_{mech} = 0.0076$, $\dot{\varepsilon} \approx 0.0001\ s^{-1}$, $N_f = 735$; and
(3) In-phase TMF, air, $T = 150$ °C to 600 °C, $\Delta\varepsilon_{mech} = 0.0076$, $\dot{\varepsilon} \approx 0.0001\ s^{-1}$, $N_f = 220$.

These tests can be readily compared, since all three tests have similar strain ranges and strain rates, and the isothermal test was performed at the maximum temperature of the TMF cycle. Moreover, the comparisons among these tests can be attributed mostly to the strain-temperature phasing, since all other parameters are about the same.

F. *Microscopy*

After testing, specimens were sectioned longitudinally through the primary crack origin using a low-speed saw and mounted in an epoxy so that the oxide would remain intact. The mounted samples were polished with successively finer grades of abrasive paper, 6 μm and 1 μm diamond paste, and 0.05 μm alumina. These samples were then gold sputtered to prevent charging of the oxide layer in the SEM. In addition to the interrupted tests, which were examined to determine the progression of damage occurring during cycling, the post-failure oxide characteristics from most of the other fatigue-life tests performed on 1070 steel were examined. Measurements of surface oxides, oxide-filled intrusions, and cracks were obtained from these SEM micrographs and will be described in Sections III–A and B.

III. CRACK GROWTH BEHAVIOR

A. *Oxide-Induced Cracking vs Internal Intergranular Cracking*

Under isothermal and TMF conditions, oxidation and creep can influence crack growth. When the oxidation effects are dominant, the crack grows by a fatigue and oxide-induced (oxide-aided) crack growth mechanism. If creep effects are dominant, creep mechanism influences crack growth. Both oxidation and creep would increase crack growth rates and reduce the fatigue life.

Creep damage in the form of internal intergranular cracking at pearlite colony boundaries normal to the loading axis was found to be the primary cause of the

Table II. Comparison of Identical Tests Using the 1 and 2.5 Inch Extensometers

	N_f for 1 In. Air	N_f for 2.5 In. Air	N_f for 2.5 In. Helium
Isothermal fatigue:			
T = 600 °C, $\Delta\varepsilon_{mech}$ = 0.007, $\dot{\varepsilon}$ = 0.0002 s^{-1}	703	700	4874
T = 600 °C, $\Delta\varepsilon_{mech}$ = 0.010, $\dot{\varepsilon}$ = 0.0002 s^{-1}	228	381	2467
T = 600 °C, $\Delta\varepsilon_{mech}$ = 0.007, $\dot{\varepsilon}$ = 0.02 s^{-1}	2631	2931	11,528
Out-of-phase TMF:			
T = 150 °C to 600 °C, $\Delta\varepsilon_{mech}$ = 0.0076, $\dot{\varepsilon} \approx$ 0.0001 s^{-1}	735	911, 1043	2165

reduction in fatigue life observed in in-phase TMF tests. A micrograph illustrating the intergranular cracking in an in-phase TMF test is shown in Figure 7(a). These intergranular cracks are similar to the intergranular damage observed in a stress-hold creep test at 600 °C, which is shown in Figure 7(b) for comparison. Others have found similar results in polycrystalline materials for wave shapes, including isothermal tensile dwell times, isothermal slow loading-fast unloading, as well as in-phase TMF tests.[2,5,14,32,37,38,40,41,45–47] It is noted that in isothermal and out-of-phase TMF cases, transgranular cracking was observed, and in those cases, fatigue and oxidation effects were dominant.

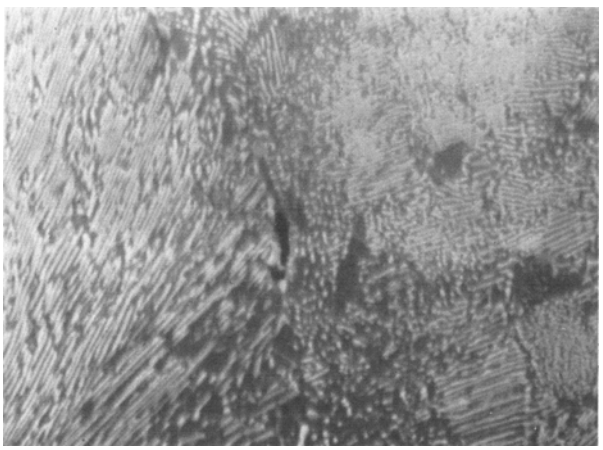

(*a*)

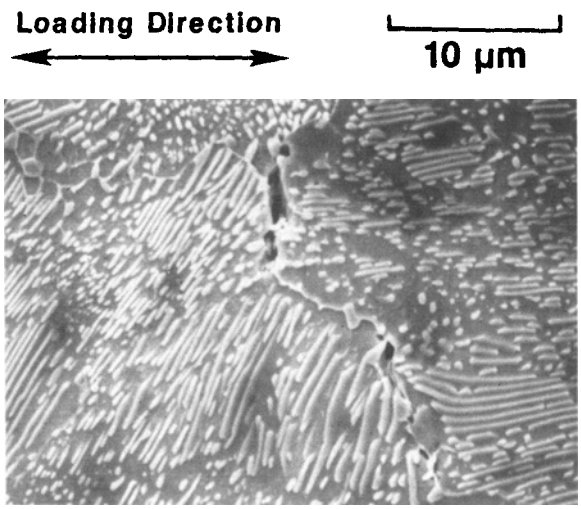

(*b*)

Fig. 7—SEM micrographs showing intergranular cracks in (*a*) in-phase TMF, T = 150 °C to 600 °C, $\Delta\varepsilon_{mech}$ = 0.0076, $\dot{\varepsilon} \approx$ 0.0001 s^{-1}, N_f = 220; and (*b*) creep test at 600 °C (5 pct Nital etch).

Above 450 °C, oxidation readily occurs in 1070 steel. Scanning electron microscope micrographs illustrating the representative surface oxide and oxide "intrusions" (surface-connected cracks filled with oxide) for the three strain-temperature phasings are shown in Figures 8(a) through (c). These micrographs in Figure 8 were taken at the same magnification at 80 pct N_f for each phasing. The metal has been etched to show the grain structure. The oxide "intrusions" in isothermal fatigue and out-of-phase TMF are transgranular. Note that no oxide intrusions formed in the in-phase TMF case. In this case, most of the damage is in the form of internal intergranular cracking at pearlite colony boundaries, as explained earlier. The mismatch of the thermal expansion coefficient between the metal and oxide showed little influence on the cracking behavior in the TMF cases. Thermal cycling under zero applied mechanical load did not cause the surface oxide to rupture.

Upon examination of oxide-induced crack growth under different laboratory testing conditions, two major types of crack growth can be differentiated. The crack tips illustrating these two types of growth are shown in Figures 9(a) and (b), which show the enlargement of the crack tips in Figures 8(b) and (a), respectively. These crack tips are filled with oxide. Note that the metal microstructure consists of pearlite lamellae and spheroidized pearlite. The Type I crack growth is characterized by a "continuous" oxide layer along the environmentally exposed surfaces including the crack faces (Figure 9(a)). Type II growth consists of oxide "intrusions" with "multilayered" or "stratified" oxide layers (Figure 9(b)). The thickness of each individual layer ranged from 0.1 to 5 μm. As discussed in Part II of this paper, this thickness depends on the strain, strain rate, temperature, and the phasing of the strain and temperature. An explanation of why a continuous oxide is formed sometimes and a stratified oxide is formed at other times is also discussed in Part II.

For a free-growing oxide on a cylindrical metal surface, Bruce and Hancock[29] predict that loss of adhesion between metal and oxide will occur at approximately 1 μm for the diameter of the specimens considered here. This loss in adhesion is due primarily to the compressive hoop stress in the oxide.[29] Other researchers have observed Type II oxides in other carbon and alloy steels.[26,35,48,49] Type II oxides that have been observed in 1070 steel

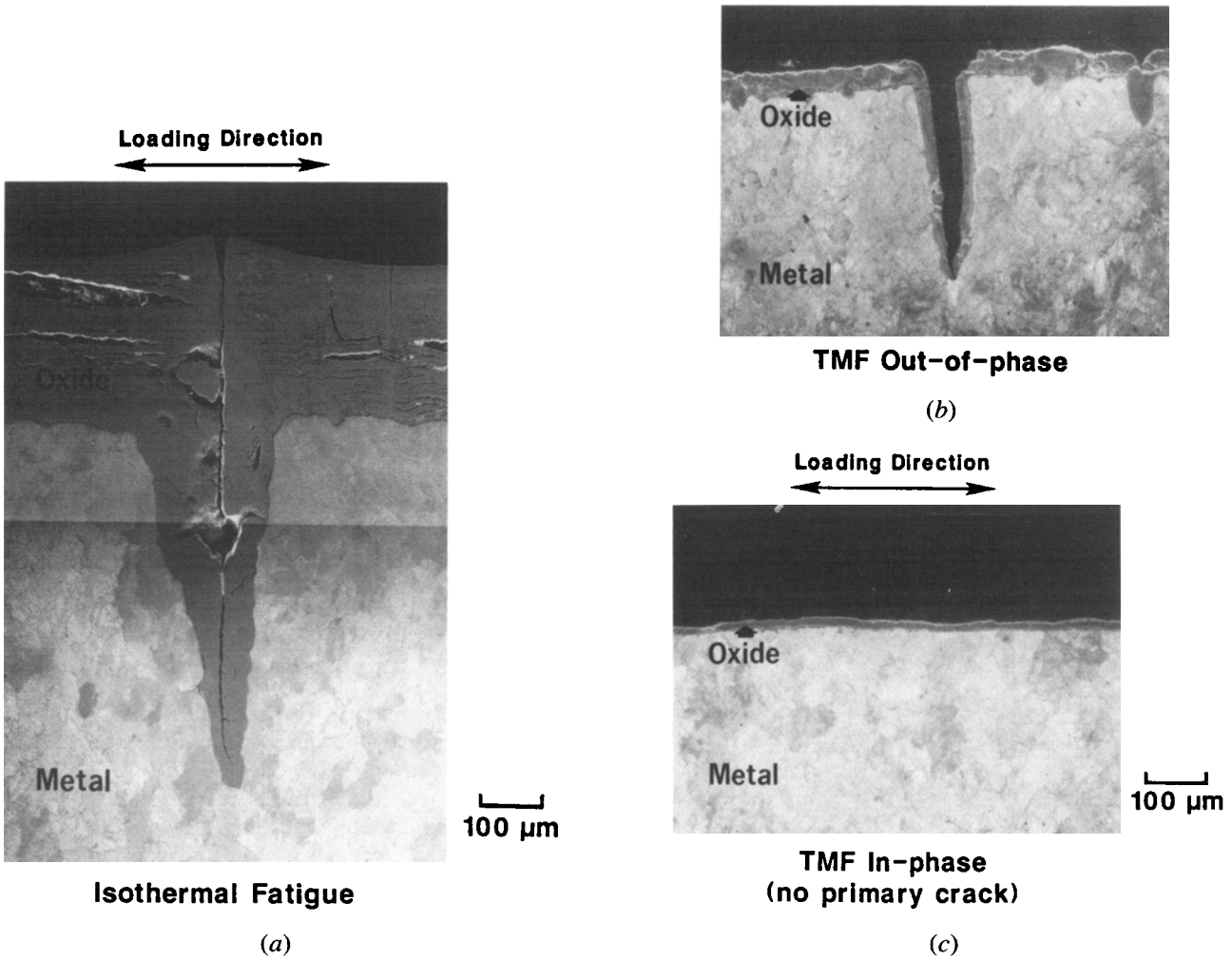

Fig. 8—SEM micrographs showing surface oxide and oxide "intrusions" for three different tests at 80 pct N_f: (*a*) isothermal fatigue, T = 600 °C, $\Delta\varepsilon_{mech}$ = 0.0070, $\dot{\varepsilon}$ = 0.0002 s^{-1}, and N_f = 700; (*b*) out-of-phase (total constraint) TMF, T = 150 °C to 600 °C, $\Delta\varepsilon_{mech}$ = 0.0076, $\dot{\varepsilon} \approx$ 0.0001 s^{-1}, and N_f = 735; and (*c*) in-phase TMF, T = 150 °C to 600 °C, $\Delta\varepsilon_{mech}$ = 0.0076, $\dot{\varepsilon} \approx$ 0.0001 s^{-1}, and N_f = 220 (5 pct Nital etch).

consist primarily of Fe_3O_4 with some Fe_2O_3, whereas Type I oxides consist of both Fe_2O_3 and Fe_3O_4.[24] A small layer of FeO is also observed at the substrate-oxide interface in tests performed at 600 °C and above, which is just above the transition temperature for FeO formation.[35]

B. *Variables Affecting Oxide-Induced Crack Growth*

The oxide morphology of all tests performed can be placed into one of three categories as follows: (a) Type I, (b) Type II, and (c) a mixture of Types I and II. Micrographs representing these typical oxide morphologies, showing both the surface and crack oxides, are shown in Figures 8(a) and (b) for Type II and Type I growth, respectively. The Type I surface oxides are generally thinner, and the intrusions are not as wide as compared to Type II. However, a single, well-defined crack usually penetrates through the Type I oxide to the substrate (Figure 9(a)). The Type II surface oxides (Figure 8(a)) are thicker and consist of many individual layers similar to Type II oxides at a crack tip (Figure 9(b)). A mixture of both Type I and Type II oxides occurring in the same test is shown in Figure 10.

The testing conditions dictate the type of oxides which grow. Oxide morphologies (Types I and II) from experimental tests are shown in separate regions on the oxide-induced crack growth behavior map shown in Figure 11. In the shaded region on this plot, a mixture of Type I and II behaviors was observed. The oxide-induced crack growth behavior map shows that as the temperature increases, the oxide morphology becomes entirely Type II. Also, as the strain rate increases, the oxide morphology becomes Type I. The effect of mechanical strain range was less apparent than temperature or strain rate, yet there was an effect when the extremes were considered. As the strain range is decreased, the growth becomes Type I. For example, as the strain range decreased to about $\Delta\varepsilon_{mech}$ = 0.0030 at 600 °C, a threshold was reached where the oxide no longer detached from the surface, and the growth was Type I with no oxide intrusions under all testing conditions. Skelton and Bucklow[48] found $\Delta\varepsilon_{mech}$ = 0.0030 to be the threshold for oxide detachment in a low alloy steel. At very small strain ranges, less than the fracture strain of the oxide, the transition from Type I to Type II oxide growth would be expected to shift to the right in Figure 11. A bounding example is free surface oxidation. For example, a

Type I

(*a*)

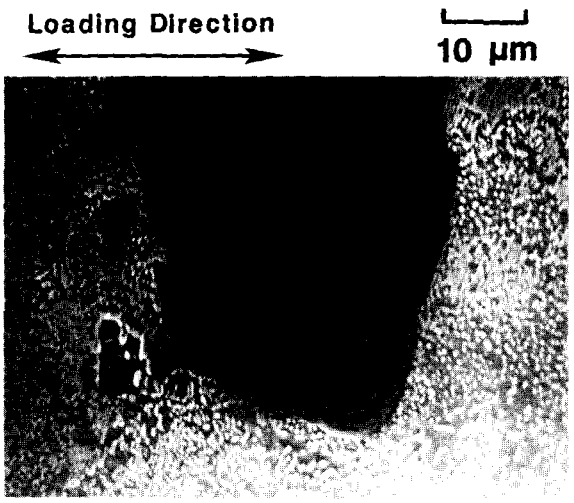

Type II

(*b*)

Fig. 9—SEM micrographs showing oxide intrusion tips resulting from (*a*) Type I growth (out-of-phase TMF, T = 150 °C to 600 °C, $\Delta\varepsilon_{mech}$ = 0.0076, and $\dot{\varepsilon} \approx 0.0001\ s^{-1}$) and (*b*) Type II growth (isothermal fatigue, T = 600 °C, $\Delta\varepsilon_{mech}$ = 0.0070, and $\dot{\varepsilon} = 0.0002\ s^{-1}$) (5 pct Nital etch).

T = 600 °C zero stress test ($\Delta\varepsilon_{mech} = 0$) produced a single-layer oxide which is representative of Type I growth.[50]

Because temperature varies during TMF testing, a method of depicting these data on the oxide-induced crack growth behavior map had to be used. Since the oxide morphology is determined by the cracking behavior of the oxide, the "effective" temperature of a TMF cycle is the temperature when the oxide would typically fracture. For the case of out-of-phase TMF (total constraint), the oxide will typically fracture near the low-temperature end of the cycle, when the oxide is more brittle and the stress is tensile. Therefore, the minimum temperature of the out-of-phase cycle is used as the testing temperature in the oxide-induced crack growth behavior map. As shown by the out-of-phase TMF data in Figure 11, there

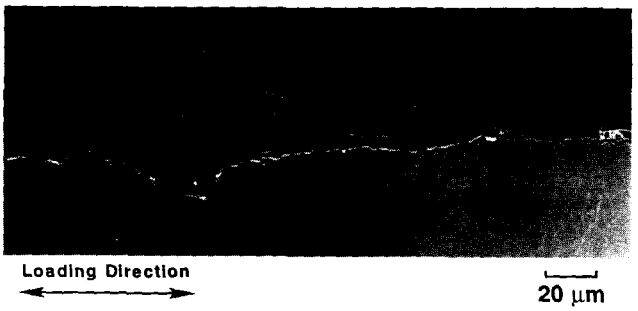

Fig. 10—SEM micrograph showing surface oxides and oxide intrusions for mixed growth (isothermal fatigue, T = 600 °C, $\Delta\varepsilon_{mech}$ = 0.010, $\dot{\varepsilon} = 0.02\ s^{-1}$, and N_f = 1062).

is clearly an oxide morphology change as the minimum (and mean) temperature is increased. For the in-phase TMF case, cracking occurred by an internal intergranular cracking mechanism and cannot be represented on the map (Figure 11).

IV. FATIGUE LIFE RESULTS

Fatigue life results for isothermal fatigue tests in 1070 steel performed at three different temperatures and three strain rates are given in Figure 12. At 400 °C (Figure 12(a)), there is little effect of strain rate on life, whereas at higher temperatures (Figures 12(b) and (c)), as the strain rate decreases, the life also decreases. At these temperatures, the fatigue life is influenced by an addition of creep and/or environmental (oxidation) damage. At 400 °C in 1070 steel, creep and oxidation are very minimal, and, consequently, the life is controlled by fatigue alone. The strain-life curve at 400 °C is nearly the same as the strain-life curve for room temperature (see Part II of this paper).

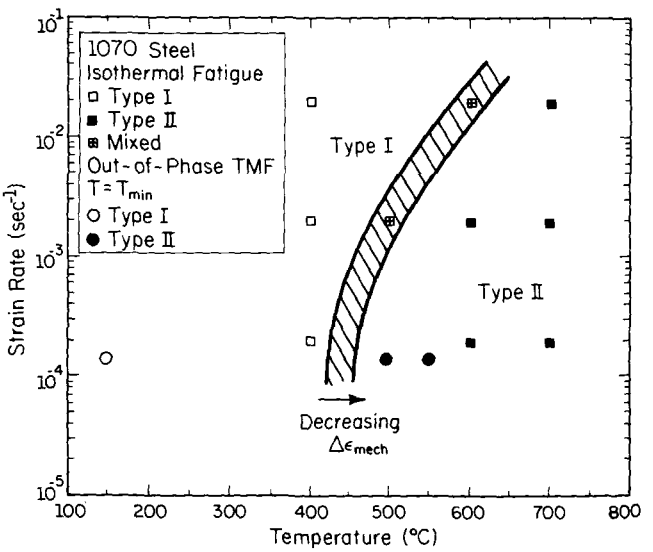

Fig. 11—Oxide-induced crack growth behavior map as a function of temperature and strain rate.

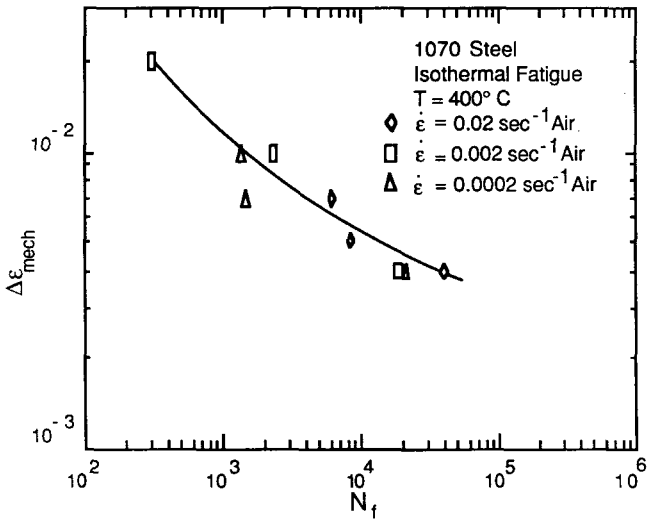

(*a*)

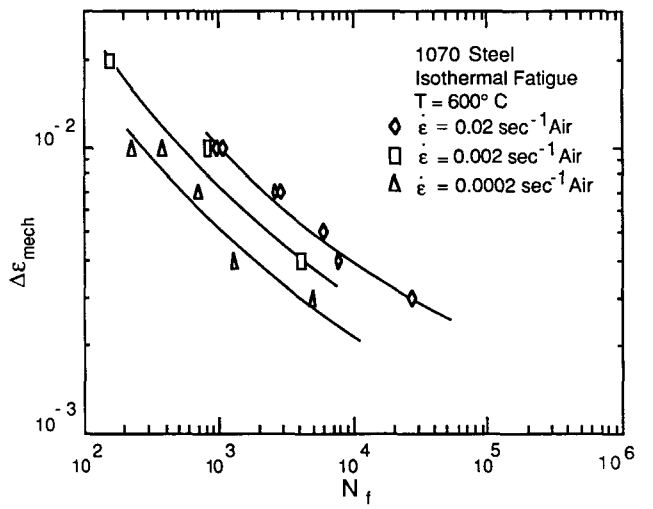

(*b*)

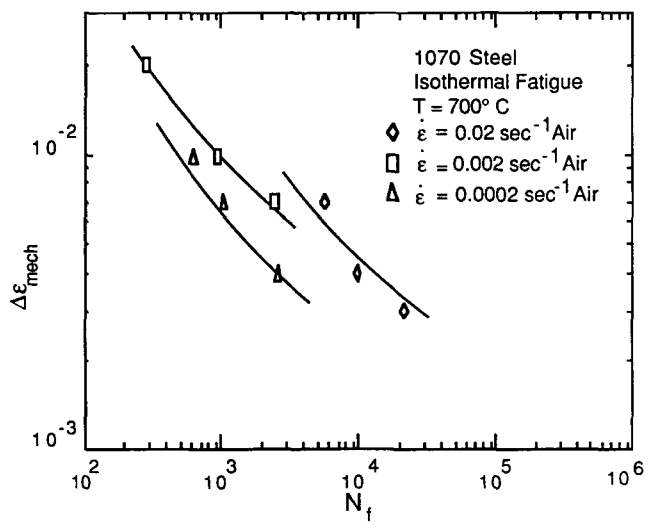

(*c*)

Fig. 12—Isothermal fatigue strain-life data for 1070 steel at (*a*) 400 °C, (*b*) 600 °C, and (*c*) 700 °C.

The 700 °C fatigue lives are longer than the 600 °C lives (compare Figures 12(b) and (c)), even though oxidation and creep mechanisms are operating at a higher rate. This anomaly is attributed to recovery and recrystallization, which occurs in this material at 700 °C.

A comparison of air and helium isothermal fatigue life data at 600 °C is given in Figure 13. The diagram includes tests performed at two strain rates in both air and helium atmospheres. The life of the isothermal helium tests were 3 to 12 times those performed in air. A greater increase in life with increasing strain rate was obtained at the lower mechanical strain ranges. The testing time was longer for these tests; therefore, the specimens in air were exposed to the environment for a longer period of time. Note that for large strain ranges, the strain rate effect in helium is very low. For other materials, no frequency effects on life have been detected under continuous cycling in a vacuum.[45] At low strain ranges, the difference in life in helium between the two strain rates is greater, indicating some creep effects on life.

Oxidation effects were eliminated and intergranular cracking was not observed for 600 °C isothermal helium tests at $\dot{\varepsilon} = 0.02\ s^{-1}$. The life data for these helium tests were nearly the same as room-temperature fatigue life data, where creep and oxidation damage do not influence the fatigue life (Figure 14). Therefore, most damage in the material occurring at elevated temperatures can be attributed to creep, the environment, or a combination of the two, since when these effects are eliminated at elevated temperatures, the life is the same as at room temperature.

Strain-life plots of the out-of-phase (total constraint) and in-phase TMF tests are shown in Figure 15. For all tests presented in the plot, the minimum temperature of the TMF cycle was kept constant at 150 °C. The upper temperature was varied, while the mechanical strain range was equal to the thermal strain range corresponding to the temperature range. The life results indicated that for large mechanical strain ranges in air, the life of the in-phase TMF is less than out-of-phase TMF. This has been primarily attributed to creep damage occurring near the

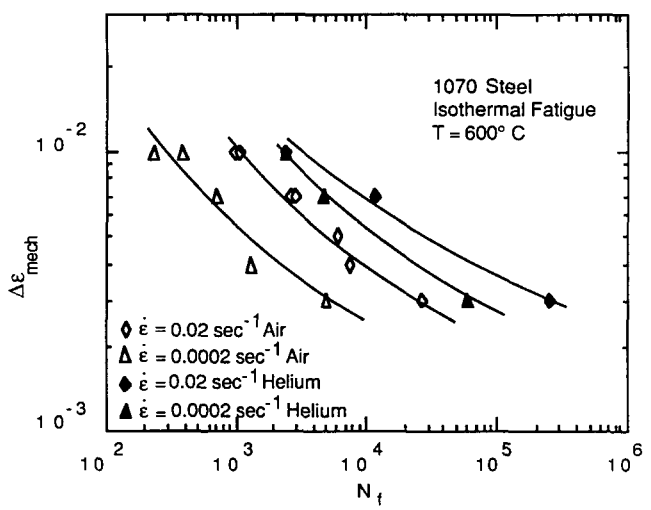

Fig. 13—Isothermal fatigue strain-life data at 600 °C for 1070 steel.

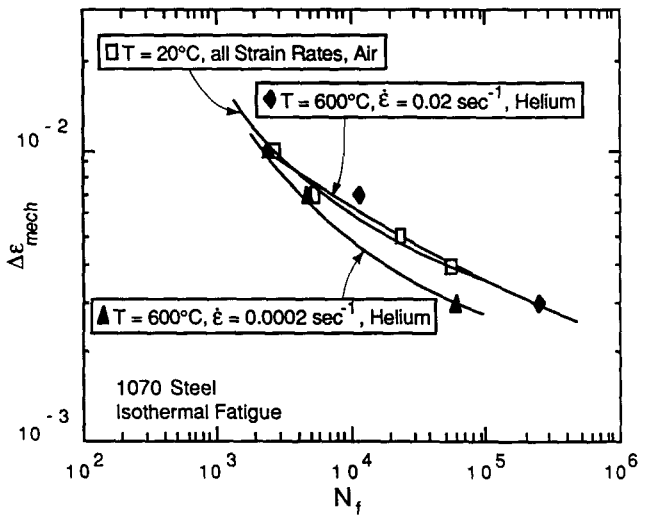

Fig. 14—Comparison of strain-life curves of helium tests performed at 600 °C to the strain-life curve at room temperature.

upper temperature, as discussed earlier in this paper. At low mechanical strain ranges, a crossover in life is observed in this material in air. The mechanism for this crossover is not established but has been observed on other materials.[51]

In addition, helium atmosphere was used in the TMF testing to eliminate the influence of oxidation on life. Thermomechanical fatigue tests performed in the helium atmosphere had a greater life but less than the increase in life observed for isothermal fatigue tests. For in-phase tests, the life in helium was only 2 times that in air. The life for out-of-phase tests in helium was about 4 times that in air. This is consistent with the fact that the in-phase tests contained creep damage along grain boundaries and lasted a shorter length of time. Environmental attack during the testing of the in-phase specimens would be less.

The progression of the primary crack growth for three

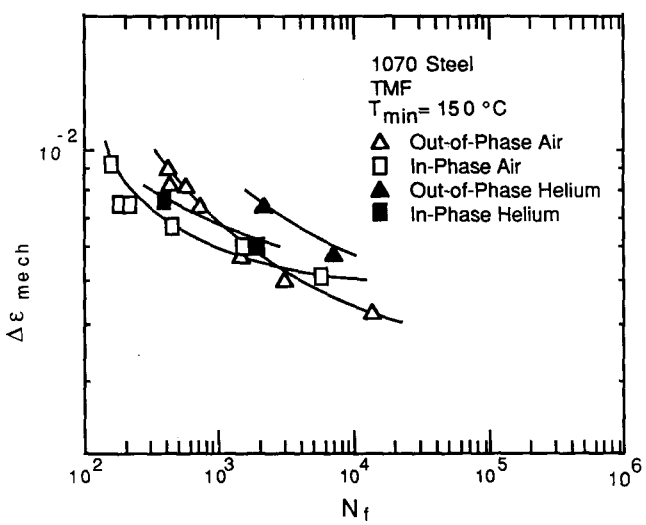

Fig. 15—Thermomechanical fatigue strain-life data for 1070 steel.

different strain-temperature phasings in air is shown in Figure 16. The crack lengths were measured from the interrupted tests described earlier. Each data point in Figure 16 represents one interrupted test. The isothermal fatigue and out-of-phase TMF curves have a similar shape. The primary crack for the in-phase TMF tests remained small for almost 80 pct of the life, and then the crack rapidly propagated to failure. At 80 pct of life, there were many intergranular cracks at the pearlite colony boundaries similar to the one shown in Figure 7. These cracks reduced the effective net section and linked up to cause the rapid crack growth.

V. DISCUSSION

To develop better and more general life prediction models, it is necessary to study microdamage mechanisms. However, this task is difficult because of the multitude of mechanisms which may operate at any one time. Therefore, the dominant damage mechanisms need to be identified, and their effect on fatigue life should be established. Damage mechanisms focused on in this study include oxidation damage and internal creep damage. These were found to be the most damaging mechanisms which reduced the fatigue life for the tests performed.

A. *Conditions Affecting Fatigue Life*

A general life prediction model should be based on the various damage mechanisms which can operate under different conditions. The fatigue life results given in this paper illustrate some important features, which must be incorporated into a general life prediction model if it is to handle many conditions.

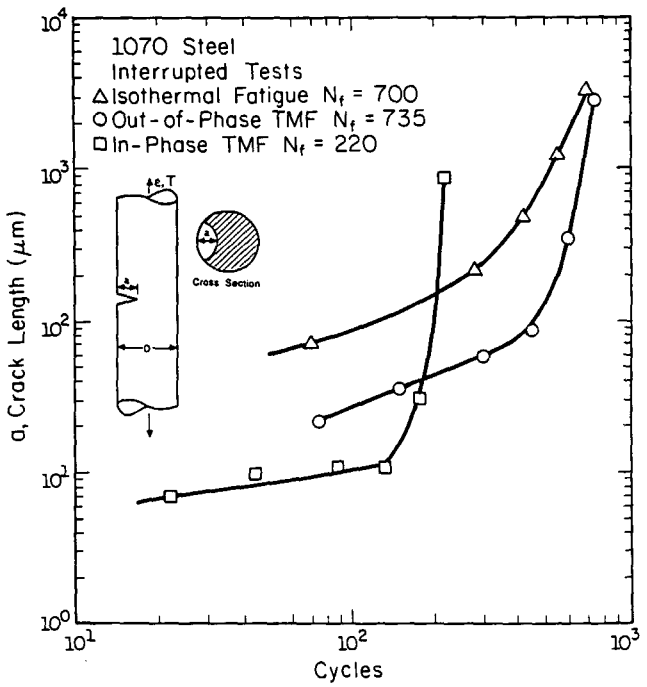

Fig. 16—Crack growth under different strain-temperature phasings in laboratory air ($\Delta\varepsilon_{mech} \approx 0.0076$, $\dot{\varepsilon} \approx 0.0001$ s^{-1}, T_{min} = 150 °C, T_{max} = 600 °C, and T (isothermal) = 600 °C).

(1) There is a strong effect of temperature on fatigue life. In general, as the temperature is increased, the fatigue life decreases, as shown by isothermal tests in Figures 12(a) and (b). An increase in temperature increases the oxidation kinetics. Since recovery mechanisms operate at 700 °C (Figure 12(c)), these would need to be incorporated into the model to account for the increase in fatigue life at that temperature.
(2) Strain rate affects both oxidation and creep damage mechanisms when the temperature is increased to above 450 °C in 1070 steel. As the strain rate is decreased, fatigue life has been shown to significantly decrease (Figures 12(b) and (c)). The oxidation mechanism is enhanced by slower strain rates, allowing more oxidation at the crack tips and on the surface. Also, creep damage can occur at lower strain rates and during dwell periods. This is apparent in helium data shown in Figure 14 in which fatigue life decreases as strain rate decreases. At low mechanical strain ranges, there is significant strain rate effect on life; however, as strain range is increased, the strain rate effect on life becomes small, indicating little creep damage is occurring. When strain range is large, test time is small even for lower strain rates, and the final failure is not controlled by time-dependent damage.
(3) The applied mechanical strain range is the underlying cause of fatigue damage, when all other damage mechanisms are absent. However, the strain range is also shown to affect the "oxide-induced crack growth type." During oxide-induced crack growth, a mechanical strain in the oxide is necessary for oxide rupture. As the mechanical strain in the oxide increases, the occurrence of brittle oxide rupture is facilitated, and fatigue life is reduced.
(4) One important feature which is often not included in prediction models is the effect of the strain-temperature phasing. For example, damage occurring during in-phase TMF tests is typically creep-dominated, which is shown by helium in-phase tests that have fatigue lives not much greater than the air tests (Figure 15); however, for out-of-phase TMF and isothermal fatigue conditions, the difference in fatigue life between air and helium atmosphere tests is much greater, indicating an oxidation-dominated damage mechanism. The crack growth rates for different strain-temperature phasings (Figure 16) verify these observations. For the in-phase TMF case, there are few surface cracks (illustrated in Figure 16 by a shorter crack size during most of the fatigue life), and the surface cracks (oxide-induced cracks) of the out-of-phase TMF and isothermal fatigue tests are longer than those in in-phase TMF throughout most of the life. This indicates that the damage accumulation for the two phasings must be different. In the in-phase TMF case, crack and void coalescence occur and cause failure at the latter part of life.
(5) The atmosphere is also important and could be implemented in a life prediction model. For example, an oxidation damage mechanism would not operate in an inert atmosphere such as helium (or at low partial pressures of oxygen) but would be expected to operate at an increasing rate as the oxygen pressure is increased in the atmosphere, and a reduction in fatigue life would typically occur (Figures 13 and 15). In addition, a general life prediction model could incorporate the effects of other gas or liquid environments.

B. *Oxidation Damage Mechanisms*

Oxidation damage mechanisms include (a) crack nucleation in surface oxides and (b) oxide-induced crack growth. Crack nucleation is defined as the rupture of the first surface oxide layer. Oxide-induced crack growth is described as the repeated formation of an oxide layer at the crack tip and its rupture, exposing fresh metallic material to the environment. Since nucleation is a one-time event that occurs early in the life (Figure 16), it is more relevant to develop an oxidation damage model based on the oxide-induced crack growth which occurs continuously during the life.

A model describing these oxidation damage mechanisms must include the factors which will affect the nucleation of cracks in the surface oxide and the oxide-induced crack growth at crack tips. It has been shown that temperature, strain rate, strain range, and strain-temperature phasing all play a significant role in determining the type of oxide growth. From a modeling standpoint, it is important to identify the similarities between Type I and Type II oxides, so that a model may be developed which is general enough to handle both cases. For example, one way that two oxide types may be unified is by considering the thickness of the oxide when it ruptures. For Type I oxides, the critical thickness of the oxide layer attached to the substrate at rupture is small (less than 0.1 μm), and the oxide does not detach from the surface after rupture. Consequently, long continuous oxides are observed on the crack surfaces, as shown in Figure 9(a). Type II oxides rupture when the thickness of the oxide layer attached to the substrate is greater (around 1 μm). In this case, the oxide detaches from the substrate, and the total oxide thickness is much greater. By utilizing this critical thickness for oxide rupture in different oxide types in a model, both types of oxides (Type I and Type II) can be represented by the same model. Furthermore, all the factors which affect the oxide-induced crack growth (*i.e.*, temperature, strain rate, mechanical strain range, and strain-temperature phasing) can be linked to the critical oxide thickness at rupture. A further description and implementation of this model is included in Part II of this paper.

C. *Creep Damage Mechanisms*

Creep damage observed in 1070 steel consists of internal intergranular cracks along pearlite colony boundaries perpendicular to the loading direction. These cracks become detectable (approximately 1 μm in length) at 60 pct N_f in the in-phase TMF case, where damage is creep-dominated. These cracks continue to grow until rapid crack growth commences by linkup of the intergranular cracks. The in-phase TMF curve in Figure 16 indicates that the surface damage (crack size) is small, yet rapid fracture occurs before the oxidation-dominated tests (out-of-phase TMF and isothermal fatigue) fail, even though the surface-connected cracks of these tests are much greater in size throughout most of the life.

A method for determining the amount of creep damage is required for a life prediction model. In order to do this, all other possible damage mechanisms had to be eliminated or reduced. Tests in helium atmosphere eliminated any oxidation damage. By determining the strain-life curves for 600 °C helium tests at two strain rates (Figure 14), an estimate of the creep damage contribution associated with each strain rate can be determined by examining the differences in fatigue life between these two strain rates. With increasing strain rate, little creep damage is occurring, and the 600 °C helium strain-life curve approaches the room temperature strain-life curve (Figure 14). Also, as the strain range increases, the test time decreases, and the fatigue life is no longer affected by the time-dependent creep damage mechanism. Using this information, a prediction model based on temperature, strain rate, strain-temperature phasing, and the stress history, which is a function of the strain history, can be developed. A model based on these factors is presented in Part II of this paper.

VI. SUMMARY

1. Various testing conditions at different temperatures, strain rates, mechanical strain ranges, and strain-temperature phasings were examined. Isothermal fatigue tests were performed under three strain rates in air and two strain rates in helium atmospheres. Also, in-phase and out-of-phase TMF test results were presented for both air and helium atmospheres. The fatigue lives in the helium atmospheres were greater than their air counterparts in all cases. However, percentage increase in life was much less for TMF testing than that for isothermal fatigue testing.
2. A test procedure for performing isothermal and TMF in an inert atmosphere (helium) was described. The gage section of the specimen was enclosed by a bellows with the inert atmosphere entrapped inside. Little additional equipment was required to perform these tests.
3. From an extensive study of oxide morphologies both on the surface and at crack tips, two major types of oxide growth were described. Type I oxides are continuous along the environmentally exposed surfaces, whereas Type II oxides are multilayered, and each layer is of the order of 1 μm in thickness. Both types of oxide growth resulted in transgranular crack growth in isothermal fatigue and out-of-phase TMF conditions.
4. Under in-phase TMF conditions, internal intergranular cracking was observed at pearlite colony boundaries perpendicular to the loading axis.
5. It was shown that oxidation and creep damage mechanisms are two primary mechanisms which will enhance fatigue damage. Experimental results indicate that many factors significantly influence the severity of these mechanisms. These include temperature, strain rate, mechanical strain range, and strain-temperature phasing. These factors must be incorporated into a life prediction model to provide a general and unifying approach to handling many conditions.

ACKNOWLEDGMENTS

This work is supported by the Association of American Railroads, Technical Center, Chicago, IL. The cooperation of Dr. Daniel Stone, Director of Metallurgy, and Mr. Michael Fec, Senior Engineer, is appreciated.

REFERENCES

1. C.E. Jaske: ASTM STP 612, D.A. Spera and D.F. Mowbray, eds., 1976, pp. 170-98.
2. K.D. Sheffler: ASTM STP 612, D.A. Spera and D.F. Mowbray, eds., 1976, pp. 214-26.
3. M.L. Karasek: *Materials Engineering-Mechanical Behavior*, Report No. 132, College of Engineering, University of Illinois at Urbana-Champaign, Aug. 1986.
4. R.S. Nelson, J.F. Schoendorf, and L.S. Lin: *Creep Fatigue Life Prediction for Engine Hot Section Materials (Isotropic)-Interim Report*, NASA Contractor Report 179550, Dec. 1986.
5. S. Majumdar: *Thermal Stress, Material Deformation, and Thermo-Mechanical Fatigue*, H. Sehitoglu and S.Y. Zamrik, eds., ASME, New York, NY, 1987, PVP-vol. 123, pp. 31-36.
6. Gary R. Halford: in *Thermal Stresses II*, R.B. Hetnarski, ed., 1987, pp. 330-428.
7. J. Gayda, T.P. Gabb, R.V. Miner, and G.R. Halford: *Bithermal Low-Cycle Fatigue Behavior of a NiCoCrAlY-Coated Single Crystal Superalloy*, NASA TM-89831, 1987.
8. Stephen D. Antolovich, R. Baur, and S. Liu: *Superalloys 1980*, J.K. Tien, S.T. Wlodek, H. Morrow III, M. Gell, and G.E. Maurer, eds., ASM, Metals Park, OH, 1980, pp. 605-13.
9. K.D. Challenger, A.K. Miller, and C.R. Brinkman: *J. Eng. Mater. Tech.*, Trans. ASME, 1981, vol. 103 (1), pp. 7-14.
10. J. Bressers, U. Schusser, and B. Ilschner: *Low Cycle Fatigue and Elasto-Plastic Behaviour of Materials*, 2nd Int. Conf. on Low Cycle Fatigue and Elasto-Plastic Behaviour of Materials, Munich, Germany, Elsevier Applied Science Publishers Ltd., Barking, U.K., 1987, pp. 365-70.
11. S. Floreen and R.H. Kane: *Fatigue of Engineering Materials and Structures*, 1980, vol. 2, pp. 401-12.
12. H.W. Liu and Y. Oshida: *Theoretical and Applied Fracture Mechanics*, 1986, vol. 6, pp. 85-94.
13. J. Reuchet and L. Rémy: *Metall. Trans. A*, 1983, vol. 14A, pp. 141-49.
14. S. Majumdar and P.S. Maiya: *J. Eng. Mater. and Tech.*, 1980, vol. 102, pp. 159-67.
15. B. Kirkwood and J.R. Weertman: *Micro and Macro Mechanics of Crack Growth*, K. Sadananda, B.B. Rath, and D.J. Michel, eds., TMS-AIME, 1982, pp. 199-212.
16. John Wareing: *Metall. Trans. A*, 1977, vol. 8A, pp. 711-21.
17. S. Baik and R. Raj: *Metall. Trans. A*, 1982, vol. 13A, pp. 1207-14.
18. B.K. Min and R. Raj: *Acta Metall.*, 1978, vol. 26, pp. 1007-22.
19. B. Tomkins: in *Creep and Fatigue in High Temperature Alloys*, J. Bressers, ed., 1981, pp. 111-43.
20. J.K. Tien, S.V. Nair, and V.C. Nardone: in *Flow and Fracture at Elevated Temperatures*, Rishi Raj, ed., ASM, Metals Park, OH, 1985, pp. 179-213.
21. D. Bruce and P. Hancock: *J. Inst. of Metals*, 1969, vol. 97, pp. 148-55.
22. J.K. Tien and J.M. Davidson: *Stress Effects and the Oxidation of Metals*, John V. Cathcart, ed., TMS-AIME, 1974, pp. 200-19.
23. H. Riedel: *Met. Sci.*, 1982, vol. 16 (12), pp. 569-74.
24. Huseyin Sehitoglu and M. Karasek: *J. Eng. Mat. Tech.*, Trans. ASME, 1986, vol. 108 (4), pp. 192-98.
25. N.B. Pilling and R.E. Bedworth: *J. Inst. of Metals*, 1923, vol. 29, pp. 529-82.
26. J.E. Forrest and P.S. Bell: *Corrosion and Mechanical Stress at High Temperatures*, V. Guttmann and M. Merz, eds., Applied Science Publishers Ltd., London, 1981, pp. 339-58.
27. A. Atkinson: *Corros. Sci.*, 1982, vol. 22 (4), pp. 347-57.
28. M. Schutze: *Oxid. Met.*, 1985, vol. 24 (3/4), pp. 199-232.

29. D. Bruce and P. Hancock: *J. Iron Steel Inst.*, Nov. 1970, pp. 1021-24.
30. M.I. Manning: *Corros. Sci.*, 1981, vol. 21 (4), pp. 301-16.
31. L.F. Coffin, Jr.: *Metall. Trans.*, 1972, vol. 3, pp. 1777-88.
32. R.P. Skelton: *Low-Cycle Fatigue and Life Prediction*, ASTM STP 770, C. Amzallag, B.N. Leis, and P. Rabbe, eds., 1982, pp. 337-81.
33. R.H. Cook and R.P. Skelton: *Int. Metall. Rev.*, 1974, vol. 19 (12), pp. 199-222.
34. C.H. Wells, P.S. Follansbee, and R.R. Dils: *Stress Effects and the Oxidation of Metals*, John V. Cathcart, ed., TMS-AIME, 1974, pp. 220-44.
35. G. Ward, B.S. Hockenhull, and P. Hancock: *Metall. Trans.*, 1974, vol. 5, pp. 1451-55.
36. D.S. Wood, G. Slattery, J. Wynn, D. Connaughton, and M.E. Lambert: *The Influence of Environment on Fatigue*, The Institution of Mechanical Engineers, 1977, pp. 11-20.
37. P.S. Maiya: *Mater. Sci. and Eng.*, 1981, vol. 47, pp. 13-21.
38. D.J. Michel and H.H. Smith: *Res Mechanica*, 1985, vol. 14, pp. 271-85.
39. R.P. Skelton: *Mater. Sci. and Eng.*, 1978, vol. 35, pp. 287-98.
40. C.R. Brinkman: *Int. Metals Rev.*, 1985, vol. 30 (5), pp. 235-58.
41. E. Renner, H. Vehoff, H. Riedel, and P. Neumann: *Low Cycle Fatigue and Elasto-Plastic Behaviour of Materials*, 2nd Int. Conf. on Low Cycle Fatigue and Elasto-Plastic Behaviour of Materials, Munich, Germany, 1987, pp. 277-83.
42. H. Sehitoglu, and J.D. Morrow: in *Thermal and Environmental Effects in Fatigue: Research-Design Interface*, C.E. Jaske, S.J. Hudak, Jr., and M.E. Mayfield, eds., 1983, PVP-vol. 71, pp. 93-109.
43. Huseyin Sehitoglu: *J. Eng. Mater. Tech.*, Trans. ASME, 1985, vol. 107 (7), pp. 221-26.
44. Huseyin Sehitoglu: *Engineering Fracture Mechanics*, 1987, vol. 26 (4), pp. 475-89.
45. L.F. Coffin: *Proc. Int. Symp. on Low-Cycle Fatigue Strength and Elasto-Plastic Behavior of Materials*, 1979, pp. 9-24.
46. C. Levaillant and A. Pineau: *Low-Cycle Fatigue and Life Prediction*, ASTM STP 770, C. Amzallag, B.N. Leis, and P. Rabbe, eds., 1982, pp. 169-93.
47. Ashok Saxena and John L. Bassani: *Fracture: Interactions of Microstructure, Mechanisms and Mechanics*, Joseph M. Wells and John D. Landes, eds., TMS-AIME, 1984, pp. 357-83.
48. R.P. Skelton and J.I. Bucklow: *Met. Sci.*, 1978, vol. 12 (2), pp. 64-70.
49. L. Berchtold, H.G. Sockel, and B. Ilschner: *Behaviour of High Temperature Alloys in Aggressive Environments*, 1979, pp. 927-37.
50. M. Karasek, H. Sehitoglu, and D. Slavik: ASTM STP 942, 1988, pp. 184-205.
51. Dennis A. Boismier: M.S. Thesis, University of Illinois at Urbana-Champaign, Urbana, IL, 1988.